An Annual "Urban Core-Suburban-Rural" Triad Structure Dataset for China From 1992 to 2021

Biao Xiong, Yaohuan Huang, Mingxing Chen, Chengbin Wu, *Student Member, IEEE*, and Hongyan Ren

***Abstract*—China has experienced a rapid urbanization over the past three decades, resulting in a prominent "urban core-suburban-rural" (USR) triad structure of human settlements. The USR disparities, which are related to the spatial variations of human activity intensity, have significant impacts on the spatiotemporal variations in various environmental issues such as carbon dioxide (CO_2) emissions, carbon storage, water quality, etc. However, there is a lack of national-level, long-term USR dataset compared to the large number of "Urban-Rural" dual-structure datasets. In this study, an annual USR dataset from 1992 to 2021 in China is delineated by using the nighttime light data, which is the first full coverage, long-term USR dataset of China. The consistency with other remote sensing products (global urban boundaries) and socio-economic data (demographic and point of interest data) demonstrates that the USR dataset is reliable for characterizing the spatial extents of human settlements with distinct socio-economic activity intensities. The USR maps have shown that the Chinese urban core area increased 9-fold from 16,500 km^2 in 1992 to 165,000 km^2 in 2021. The application of USR data in Fossil Fuel Combustion CO_2 (ffco2) emissions indicates that ffco2 emissions in urban core, suburban, and rural area increased 1.34, 0.36, and 0.17 billion of tons from 2000 to 2019 in China, respectively. The dataset can be used for other environmental research issues in China, which has not been possible before because of the lack of the long-term USR triad structure of human settlements.**

***Index Terms*—China, dataset, nighttime light (NTL), urban core-suburban-rural (USR), urbanization.**

I. Introduction

URBANIZATION is one of the leading concerns around the world today, which may lead to various environmental problems, such as the excessive pollution discharge [1], [2], heat island [3], [4], [5], and so on. As urbanization has been linked to human activities, such as the population and economic growth [6], the human settlement expansion, and the related land use changes [7], [8], [9], many environmental issues vary widely in places with different urbanization levels. Among these influences, the urban-rural disparities of development and landscape are considered as the initial impetus of several significant environmental factors that change along the urban-rural gradient, such as carbon storage [10], CO_2 emissions [11], antibiotic contamination [12], non-point source water pollution [13], residential greenness [14], organochlorine pesticides [15], bioavailability of toxic elements [16], household greenhouse-gas footprints [17], and so on. Therefore, a long-term dataset of human settlement that can accurately delineate the urbanization process, including the development of high-density cities, the suburban sprawl, and the expansion of exurban areas at the urban-rural fringe, is significant for achieving sustainable development goals in the constantly changing world with complex human-environment interactions [18].

As one of the most populous countries in the world, China has experienced rapid urbanization over past three decades, which has intensified the interaction between the urban core areas and the urban periphery (suburban or rural areas) and has resulted in a significant "urban core-suburban-rural" (USR) triad structure in China [19]. Being different from the urban core and rural areas, the suburban area is an urban-rural transitional areas and have both urban and rural characteristics. Identifying the spatiotemporal variation of environmental elements in the suburban area, such as water [13], soil [15], air [11], ecosystems [10], and so on, has caused wide public concerns, which is a prerequisite for improving environmental quality and guiding pollution control efforts. Furthermore, the three USR subcategories with distinct human activity intensities play diverse roles in various fields, such as functions of terrestrial ecosystems [20], climate change [21], [22], energy consumption [23], [24], population, medical treatment, and policy [25], [26], [27], [28]. However, recent datasets commonly include only one subcategory (generally urban) in the USR structure or roughly categorize the USR as one land use type, namely, artificially impervious area or residential area. It provides less information on the growing interface conflicts among urban core, suburban, and rural areas, and is insufficient to reveal the environmental influence of USR disparities. The long time-series USR dataset is the basis for further identifying USR disparities impacts on global change and sustainable development [29], [30].

Manuscript received 24 October 2023; revised 22 November 2023; accepted 6 December 2023. Date of publication 11 December 2023; date of current version 29 December 2023. This work was supported in part by the Science & Technology Fundamental Resources Investigation Program under Grant 2023FY101002 and Grant 2023FY101001 and in part by the Strategic Priority Research Program of the Chinese Academy of Sciences under Grant XDA23100301 and Grant XDA20010203. *(Corresponding author: Yaohuan Huang.)*

Biao Xiong, Yaohuan Huang, Mingxing Chen, and Chengbin Wu are with the State Key Laboratory of Resources and Environmental Information Systems, Institute of Geographic Sciences and Natural Resources Research, Chinese Academy of Sciences, Beijing 100101, China, and also with the College of Resource and Environment, University of Chinese Academy of Sciences, Beijing 100049, China (e-mail: xiongbiao3691@igsnrr.ac.cn; huangyh@lreis.ac.cn; chenmx@igsnrr.ac.cn; wucb@lreis.ac.cn).

Hongyan Ren is with the State Key Laboratory of Resources and Environmental Information Systems, Institute of Geographic Sciences and Natural Resources Research, Chinese Academy of Sciences, Beijing 100101, China (e-mail: renhy@igsnrr.ac.cn).

Digital Object Identifier 10.1109/JSTARS.2023.3341390

TABLE I
DATA SOURCES

NAME	TYPE	DOWNLOAD LINK
DMSP-OLS Nighttime Light	Raster 30 arc-second (~1000m at the Equator)	https://www.ngdc.noaa.gov/eog/dmsp/downloadV4composites.html
NPP-VIIRS Nighttime Light	Raster 15 arc-second (~500m at the Equator)	https://eogdata.mines.edu/nighttime_light/annual/v20/
Chinese prefecture-level division	Vector	https://www.webmap.cn/commres.do?method=result100W
Global Urban Boundaries (GUB)	Vector	http://data.ess.tsinghua.edu.cn/gub.html
Gridded Population of the World (GPW), v4	Raster 30 arc-second (~1000m at the Equator)	https://sedac.ciesin.columbia.edu/data/set/gpw-v4-population-density-rev11/data-download
Point of Interest (POI)	Vector	https://lbs.amap.com/api/webservice/guide/api/search
Open-Data Inventory for Anthropogenic Carbon dioxide (ODIAC)	Raster 30 arc-second (~1000m at the Equator)	https://db.cger.nies.go.jp/dataset/ODIAC/DL_odiac2020b.html

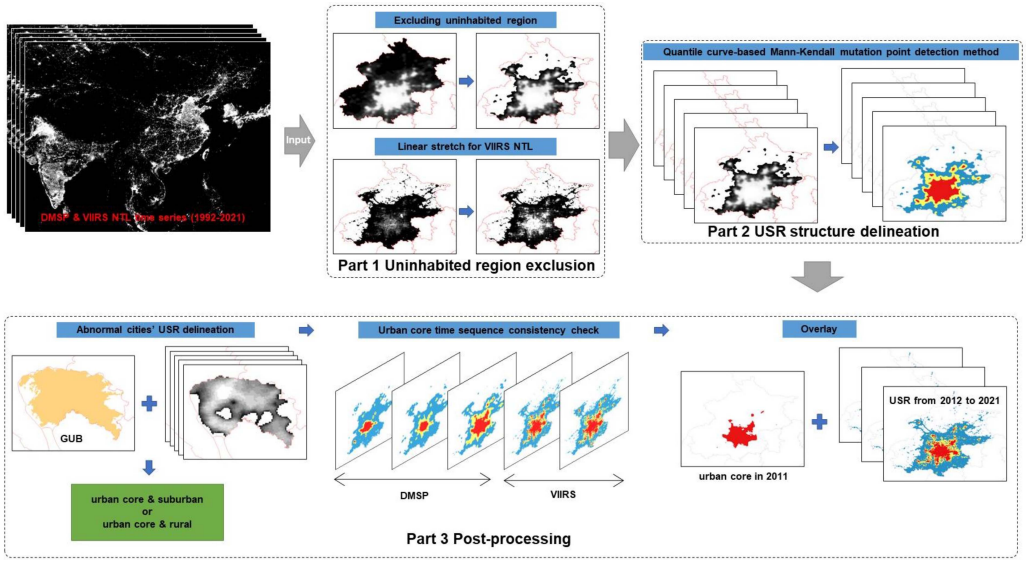

Fig. 1. Flowchart for mapping USR spatial distribution.

Over the past few decades, the satellite remote sensing data have been widely used to generate urbanization-related datasets [31]. Traditionally, the multispectral remote sensing imagery is used, including the medium spatial resolution imagery, such as Landsat, MODIS, SPOT, and CHRIS/Proba [32], [33], [34], [35], [36] and the fine resolution imagery such as IKONOS and QuickBird [37], [38]. These datasets describe artificial impervious areas based on the spectral characteristics of land use, which have contributed greatly to revealing human modifications to the landscape against the background of rapid global urbanization [18], but they are limited in their temporal coverage [39]. To address these challenges, the artificial nighttime light (NTL) images have been applied to reveal the dynamic patterns of human settlements and economic activities from different perspectives [40]. Based on the apparent NTL spatial gradient variation between urban core areas and surrounding surface types (e.g., suburban and rural) [41] due to the distinctions of human activity intensity [42], [43], [44], several regional or global datasets of human settlements have been derived from various NTL images, such as those acquired from the Defence Meteorological Satellite Program-Operational Linescan System (DMSP-OLS), the Visible Infrared Imaging Radiometer Suite (VIIRS) sensor onboard the Suomi National Polar-orbiting Partnership satellite (SNPP), and Luojia 1-01 [45], [46], [47], [48], [49]. In China, the NTL spatial gradient also helps to distinguish urban core, suburban, and rural areas, which can be applied for mapping the USR structure [31]. However, the previous datasets have mainly identified the boundary between the urban areas and the surrounding nonurban areas, such as the urban extents and the urban-rural binary classification. Furthermore, they provide less

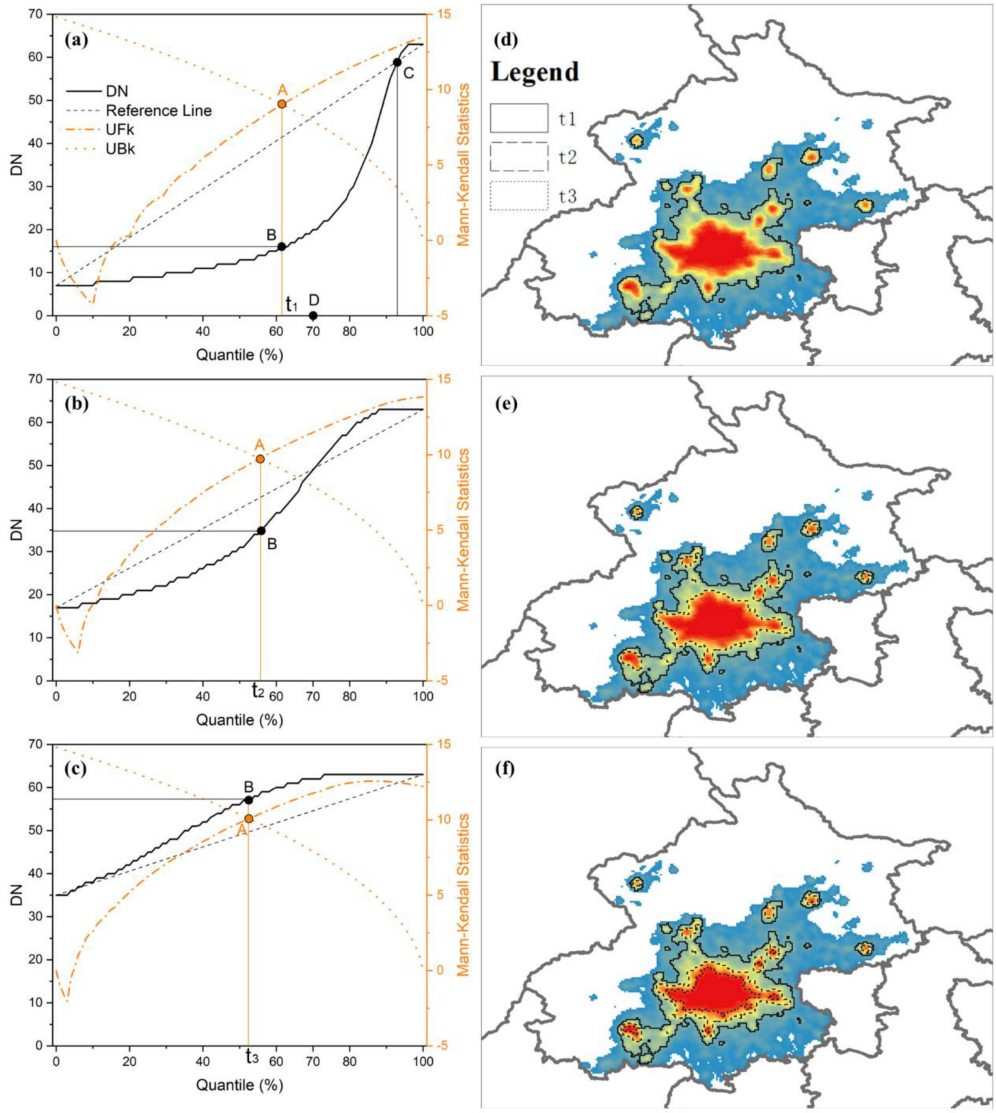

Fig. 2. Illustration of the heuristic algorithm originating from the MK mutation point detection method to obtain USR NTL thresholds. (a) First mutation point detection, point A is the intersection of MK forward sequence and backward sequence, point B is the mutation point, point C is the intersection of the reference line and the quantile curve and point D is on the *X*-axis with the coordinate 70. (b), (c) Second and third mutation point detection. (d)–(f) Corresponding USR mapping results.

information on the inner spatial structure of human settlements, namely, the USR, which hinders better identification of human developments and urbanization processes.

Among the three USR subcategories, the suburban received insufficient attention from remote sensing researchers compared to the urban and the rural, which is always considered as artificial impervious area or is confused with the urban area [50]. Considering the distinction of human activity intensity among the USR, the digital number (DN) value recorded by NTL imagery becomes a salient indicator for revealing the dynamic patterns of human settlements and socio-economic activities from different perspectives [40]. For instance, Ma et al. [51] proposed a spatially quantitative approach for partitioning DMSP-OLS NTL images into five urban subregions based on the quadratic relationship between the pixel-level NTL dataset and the corresponding NTL gradient. Later, Ma et al. [52] used a watershed segmentation algorithm and a second-order exponential decay model on VIIRS NTL data to classify human settlements. Zhou et al. [31] applied the DMSP NTL quantile curve to generate a global dataset of annual urban extents (1992–2020). Further, to extend urbanization datasets from the urban extents to the USR structures, Huang et al. [39], [58] proposed an improved multiple iterating quantile approach to delineate gradually the boundary of three USR subcategories of several typical cities in China from NTL imagery. These previous studies demonstrated that the NTL images could effectively derive USR datasets in China, whose socio-economic development is dominated by the city-level administrative unit. However, deriving a long time-series and consistent USR dataset of China from NTL images is still complicated because of the large-scale distinction in natural and socio-economic conditions at the national scale. Consequently, the lack of a USR dataset hinders the divulgence of the interior patterns of rapid urbanization in China.

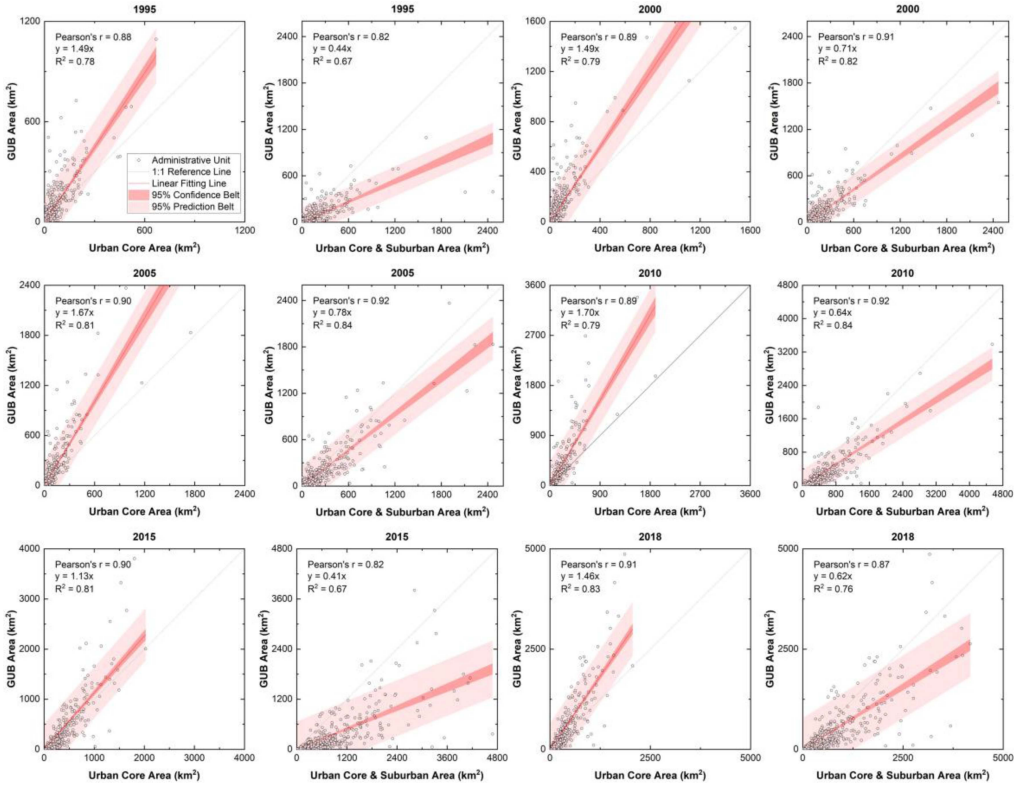

Fig. 3. Comparisons of the urban core area or the U&S area with the GUB area.

To further reveal the conflict in the interface among urban core, suburban, and rural areas that is significant to various environmental research, we generated a 1-km resolution annual USR dataset in China from 1992 to 2021 by using 30 years of NTL images acquired from DMSP and VIIRS.

The rest article has been divided as follows: Section II describes the data, Section III provides the details of the NTL-based methods for USR mapping, Section IV presents the results of comparison of the USR with artificial impervious areas, population and point of interest data (POI), Section V presents the spatiotemporal variation results of USR and the differences in fossil fuel combustion carbon dioxide emissions (ffco2) among USR and Section VI concludes this article.

II. Data

A. NTL Data

We used both DMSP-OLS (1992–2011) and SNPP-VIIRS (2012–2021) NTL images, along with the Chinese prefecture-level administrative districts data, to map the USR spatial distribution time-series dataset of every administrative unit. Both SNPP-VIIRS and DMSP-OLS acquired global NTL data in 2012 and 2013, but SNPP-VIIRS NTL data were selected because the latter exhibited better spatial and radiation resolution than the former. The DMSP-OLS NTL data (Version 4) are annual cloud-free stable composites obtained from the National Oceanic and Atmospheric Administration. The DMSP-OLS NTL products are 30 arc-seconds (∼1000 m at the Equator) grids with DN values from 0 to 63. The data are produced annually from 1992 to 2013 by six satellites (F10, F12, F14, F15, F16, and F18). Multiple satellites may acquire the global NTL imagery in the same year because they have overlapping working years. Based on the previous research [53], we selected one image obtained from one satellite per year to form a continuous unduplicated NTL series (F101992-F101994, F121995-F121996, F141997-F142003, F162004-F162009, and F182010-F182011). The SNPP-VIIRS NTL data (annual average product, Version 2), with a 15 arc-seconds (∼500 m at the Equator) spatial resolution, were obtained from the Earth Observation Group, Payne Institute for Public Policy [54]. The Chinese prefecture-level administrative districts data were obtained from the National Catalogue Service for Geographic Information in 2021 and were processed into 390 basic administrative units for consistency.

B. Auxiliary Data

To validate the USR time-series results obtained from NTL images, we used three auxiliary datasets: the global urban boundaries (GUB) [55], the Gridded Population of the World (GPW, Version 4) [56], and the POI. GUB was delineated from 30-m resolution data of global artificial impervious areas [57]. The GUB data for 1995–2018 were used to validate the USR results for the corresponding years. They were also used to map USR of some abnormal administrative units without typical USR spatial distribution (further details given in Section III-C-1). The GPW data are 30 arc-seconds (∼1000 m at the equator) grids, and the pixel values represent the population count. Considering the

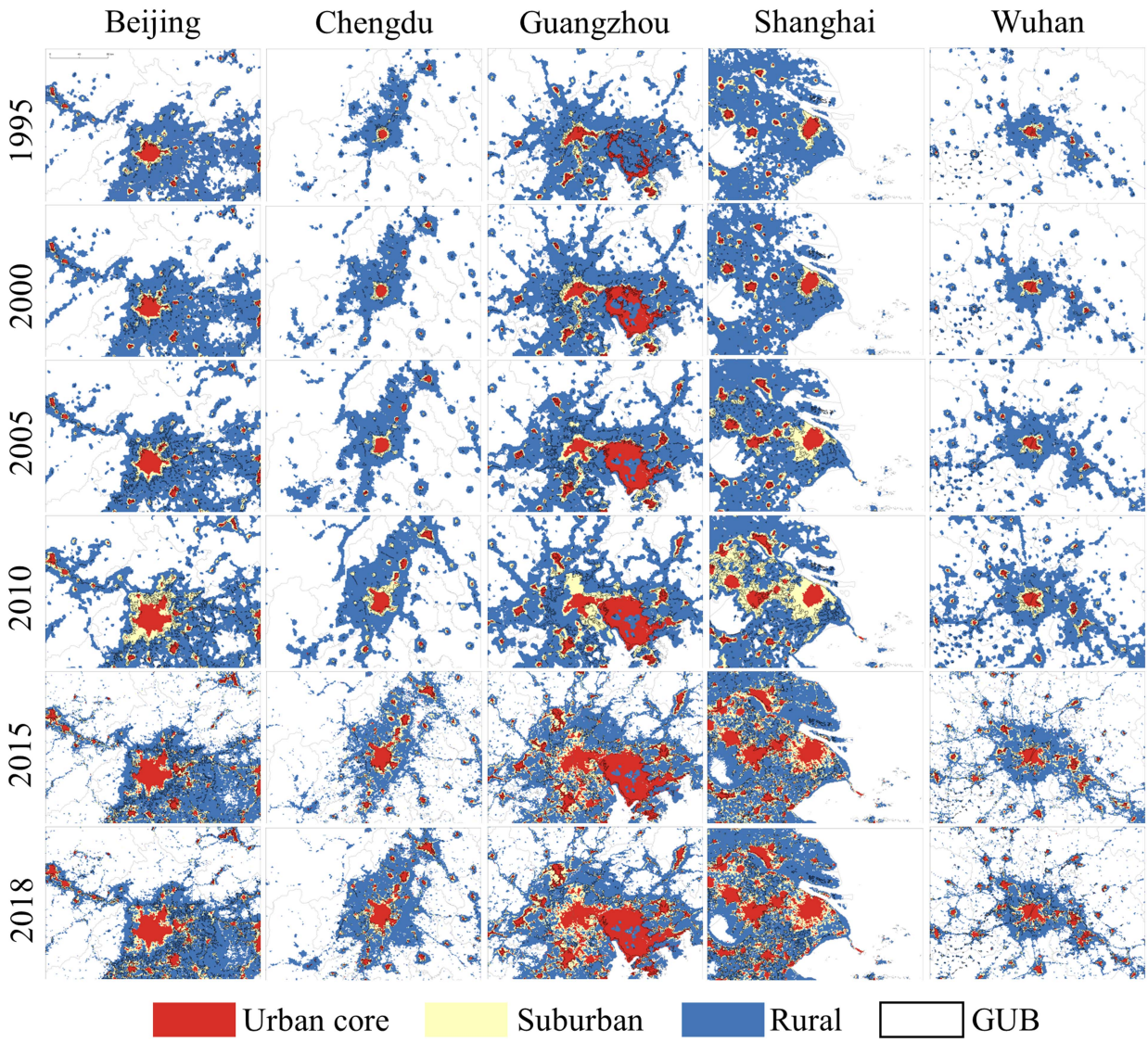

Fig. 4. Comparisons of the USR and GUB spatial extent of five certain cities.

significant relationship between the human activity intensity and the USR areas [18], we used POI to validate the USR dataset. The national POI data were obtained from Amap in 2012, 2014, and 2016, which include 20 categories covering various factors, such as economy, culture, and transportation (data for the type of public facilities are not available in 2016).

C. Environmental Issue Data

We used the open-data inventory for anthropogenic carbon dioxide (ODIAC) to investigate the total emissions and the density differences of ffco2 in the USR areas. The ODIAC is a 1-km resolution monthly global emission data product of carbon dioxide (CO_2) emissions from fossil fuel combustion, cement production, and gas flaring. The DN values are provided in the unit of tonne carbon for each grid (monthly total).

The geographic coordinate system for all the above-mentioned data is GCS_WGS_1984. The subsequent USR area calculation is based on Krasovsky_1940_Albers, which is an equal-area projected coordinate system. Table I lists the names, types, and download addresses of the data used in this study.

III. Methods

We delineated the annual USR spatial distribution (1992–2021) in China from DMSP and VIIRS NTL imagery using a quantile curve-based Mann-Kendall (MK) mutation point detection approach (see Fig. 1). It consisted of the following three parts.

1) The removal of uninhabited regions from the original NTL images.
2) The determination of the optimal USR threshold to delineate the annual USR spatial distribution for each administrative unit.
3) Postprocess of mapping the USR structure of a few abnormal administrative units and checking for the consistency of the urban core pixel time-series.

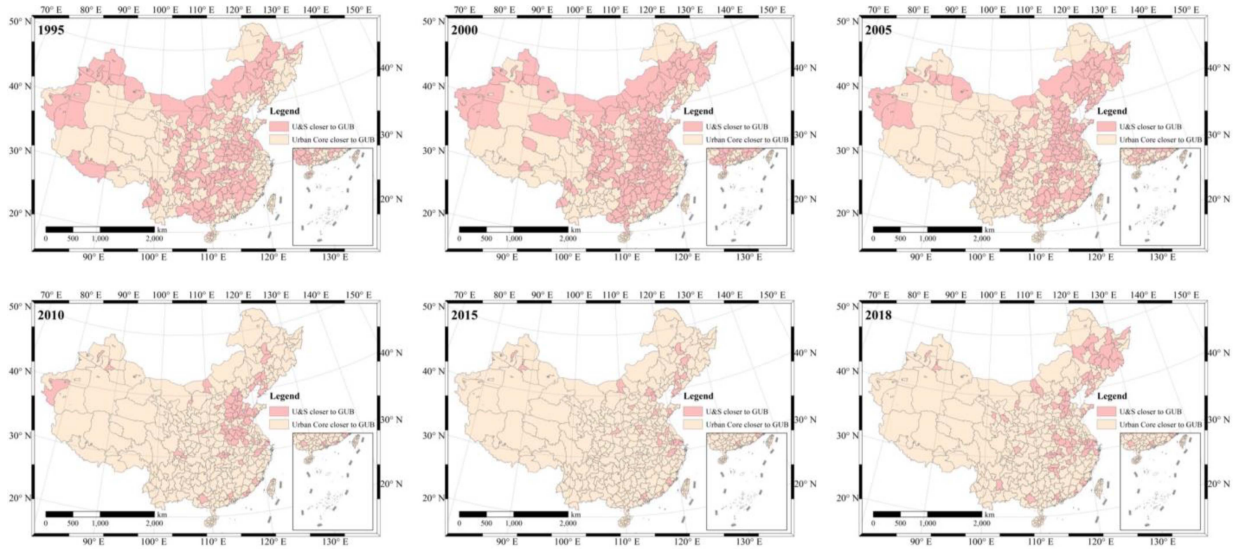

Fig. 5. Spatial distribution patterns of the relationship of the urban core area or the U&S area with the GUB area.

A. Exclusion of Uninhabited Regions

In this study, the NTL images were clipped by the Chinese prefecture-level districts to obtain separate 30-year NTL images for each administrative unit. In the DMSP NTL images, the uninhabited areas were excluded by removing pixels with small NTL values based on a quantile threshold method [58]. For the VIIRS NTL images, we used the 0-value region of the 2012 DMSP NTL image as a mask to measure the pixel value distribution of the corresponding region for 2012 VIIRS NTL image [59], which was applied on subsequent VIIRS NTL images to obtain their own thresholds. The NTL images of adjacent years were consequently visually compared to modify and determine the final threshold.

B. Delineation of the USR Structure

To determine the DN thresholds of the quantile curve that accurately distinguishes the USR in the 390 Chinese administrative units, we constructed the NTL value quantile sequence of d_i, which was ranked in the not-decreasing order. Subsequently, the sequence's mutation points were detected using the MK method. Based on the intersection point of the forward and inverse sequences, the mutation point of the original data was obtained, which was considered one of the USR thresholds.

As shown in Fig. 2, we initially detected the first mutation point [B in Fig. 2(a)] on the NTL quantile curve and recorded the obtained threshold value as t_1. Subsequently, we eliminated pixels with DN values smaller than t_1, detected the second mutation point [B in Fig. 2(b)], and recorded the second threshold value as t_2. To avoid the overestimation of urban core areas in the DMSP NTL image, we decided to detect the third mutation point [B in Fig. 2(c)] if the location of point C is on the right of point D [see Fig. 2(a)] and recorded the third threshold value as t_3. The last two obtained thresholds were taken as the optimal thresholds for the USR structure delineation. The spatial ranges corresponding to the three MK detections are shown in Fig. 2(d)–(f).

C. Postprocessing of Outlier Cities

1) Delineation of the USR of Abnormal Cities: In total, 27 administrative units were abnormal in the MK detection stage, which were caused by a low level of urbanization with very low NTL values (e.g., Sansha and Naqu cities) or a full urbanization with extremely high NTL values (e.g., Dongguan and Shenzhen cities). Namely, these abnormal administrative units present an untypical USR triad structure. For these, we determined the threshold by using the urban boundaries in the GUB data, which is estimated by

$$\text{Threshold} = \underset{i\in[\text{DN}_{\min},\text{DN}_{\max}]}{\operatorname{argmin}} \left(\text{Area}\left(\text{DN}\geq i\right)\leq \text{Area}\left(\text{GUB}\right)\right). \quad (1)$$

The threshold needs to fulfill the following condition: the area of the pixels greater than or equal to it is closest to the GUB benchmark area. And we marked these pixels as "urban core". The pixels with values less than the threshold were labeled as "suburban" or "rural". The developed cities were divided into urban core and suburban, while the underdeveloped cities were divided into urban core and rural.

2) Consistency Check for Urban Core Time-Series: To eliminate noise and ensure the rationality of the initial USR results, we performed the pixel-level postprocessing of urban core regions using a temporal consistency check. The temporal consistency check assumes that the transformation from nonurban core regions to urban core regions is irreversible [35]. First, we marked urban core pixels as 1 and other pixels as 0, obtaining a 0-1 sequence of length 30 for each position. Subsequently, a one-dimensional sliding window with a gradually increasing window radius from 1 is applied to perform a sliding check on each element of the time-series. The central element value was changed to the main element value in the window until no element changed again. According to the abovementioned process, the 30-year USR results were checked to obtain the final dataset.

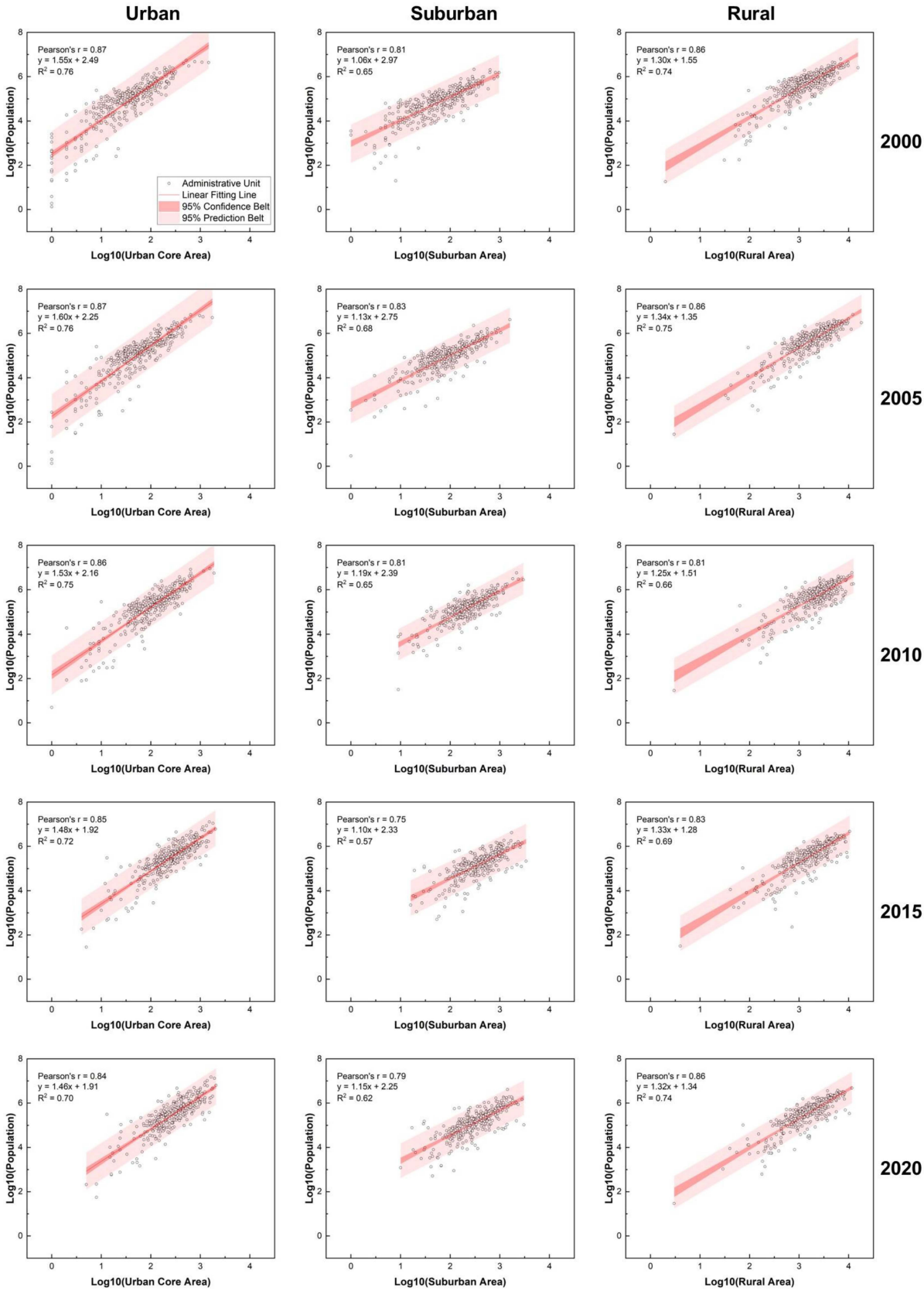

Fig. 6. Relationship between the USR areas and the population from GPW.

TABLE II
CORRELATION OF THE USR AREAS WITH THE NUMBER OF DIFFERENT POIS

	2012			2014			2016		
	urban	suburban	rural	urban	suburban	rural	urban	suburban	rural
Transportation Service (T S)	**0.70**	0.46	0.60	0.63	0.24	0.39	0.67	0.43	0.48
Accommodation Service (Ac S)	**0.78**	0.53	0.50	0.68	0.26	0.32	0.69	0.42	0.43
Sports & Recreation (S & R)	**0.76**	0.48	0.56	0.70	0.25	0.36	0.69	0.43	0.50
Public Facility (P F)	**0.67**	0.51	0.52	0.64	0.32	0.39			
Enterprises (E)	**0.74**	0.50	0.56	0.68	0.28	0.41	0.67	0.45	0.55
Medical Service (Me S)	**0.81**	0.63	0.74	0.75	0.38	0.54	0.78	0.62	0.73
Commercial House (C H)	**0.67**	0.41	0.50	0.62	0.20	0.33	0.56	0.32	0.42
Place Name & Address (P N & A)	0.82	0.78	**0.85**	0.80	0.55	0.63	0.75	0.50	0.67
Motorcycle Service (Mo S)	**0.52**	0.52	0.42	0.50	0.31	0.32	0.52	0.44	0.48
Governmental Organization & Social Group (G O & S G)	**0.83**	0.65	0.73	0.78	0.39	0.48	0.78	0.64	0.71
Auto Service (Au S)	**0.83**	0.72	0.75	0.79	0.53	0.67	0.82	0.69	0.79
Auto Repair (A R)	0.83	0.59	0.56	0.78	0.37	0.45	**0.84**	0.65	0.69
Auto Dealers (A D)	**0.86**	0.57	0.53	0.83	0.37	0.42	0.85	0.62	0.61
Daily Life Service (D L S)	**0.78**	0.54	0.64	0.72	0.32	0.49	0.75	0.53	0.69
Science/Culture & Education Service (S/C & E S)	0.76	0.64	**0.79**	0.68	0.38	0.58	0.69	0.57	0.77
Shopping (S)	**0.80**	0.53	0.55	0.75	0.31	0.45	0.77	0.57	0.67
Road Furniture (R F)	0.75	0.73	0.72	**0.77**	0.53	0.51	0.39	0.69	0.65
Finance & Insurance Service (F & I S)	**0.83**	0.64	0.78	0.76	0.40	0.55	0.76	0.63	0.73
Tourist Attraction (T A)	**0.75**	0.52	0.54	0.66	0.29	0.37	0.64	0.45	0.51
Food & Beverages (F & B)	**0.77**	0.52	0.50	0.66	0.28	0.44	0.74	0.51	0.67

The bolded numbers are the maximum values of the correlation coefficients for each type of POI with the USR areas.

IV. RESULTS AND DISCUSSION

A. Comparison With Global Urban Time-Series Products

We compared the urban core area and the urban core and suburban (U&S) area of USR results with the GUB data [55]. As shown in Fig. 3, the Pearson's correlation coefficients (r) between the urban core area and the GUB area for the six years were greater than 0.88, indicating that the urban core area was largely consistent with the intensive artificial impervious areas in China. However, the slopes of the linear fit were all greater than 1 with the coefficient of determination (R^2) values greater than 0.78, implying that the urban core area was smaller than the GUB area. Further, the r values between the total area of U&S and the GUB area were greater than 0.82, which was slightly less than that between the urban core area and the GUB area. Moreover, the slopes of the linear fit were less than 1 with the R^2 values greater than 0.67, indicating that the U&S area was generally larger than the GUB area. Although the urban core area and the U&S area were both highly consistent with the GUB area, the statistical value of U&S fluctuated more, with the r value ranging from 0.82 to 0.92 and the R^2 value ranging from 0.67 to 0.84. Thus, suburban areas could be concluded as a significantly uncertain subcategory of USR during the urbanization process. Further, the time-series analysis showed that the r and R^2 values of the urban core area and the GUB area between 2000 and 2010 were smaller than those of the U&S area and the GUB area. Moreover, the r and R^2 values of the urban core area and the GUB area increased gradually and were larger than those of the U&S area and the GUB area in 2015 and 2018. This indicated that the intense human activities are increasingly aggregated in urban core areas with rapid urbanization in China. In suburban areas, the human activities became less consistent with the increase in the artificial impervious areas, probably because of the uncontrolled urban sprawl. Then, we selected five representative cities (Beijing, Chengdu, Guangzhou, Shanghai, Wuhan) to compare the USR results and the GUB spatial extents (see Fig. 4). The GUB spatial extent is within the USR spatial extent and almost encompasses the urban core. On average, 90% of urban core pixels belong to GUB, 50% of suburban pixels belong to GUB, and rural areas are basically distributed in the periphery of GUB. This spatial consistency also shows the accuracy and rationality of our USR dataset.

To comprehensively understand the spatiotemporal variations of the urban core area and the suburban area in China, we compared the deviation of the urban core area and the U&S area from the GUB area in the 390 administrative units. As shown in Fig. 5, the number of the administrative units with the urban core area closer to the GUB area compared with the U&S area was dominant in recent years. The proportions of the administrative units with the urban core area closer to the GUB area were 81%, 92%, and 78% in 2010, 2015, and 2018, respectively, and 59%, 46%, and 57% in 1995, 2000, and 2005, respectively. This indicated that Chinese urbanization along with the economic development was concentrated in urban core areas

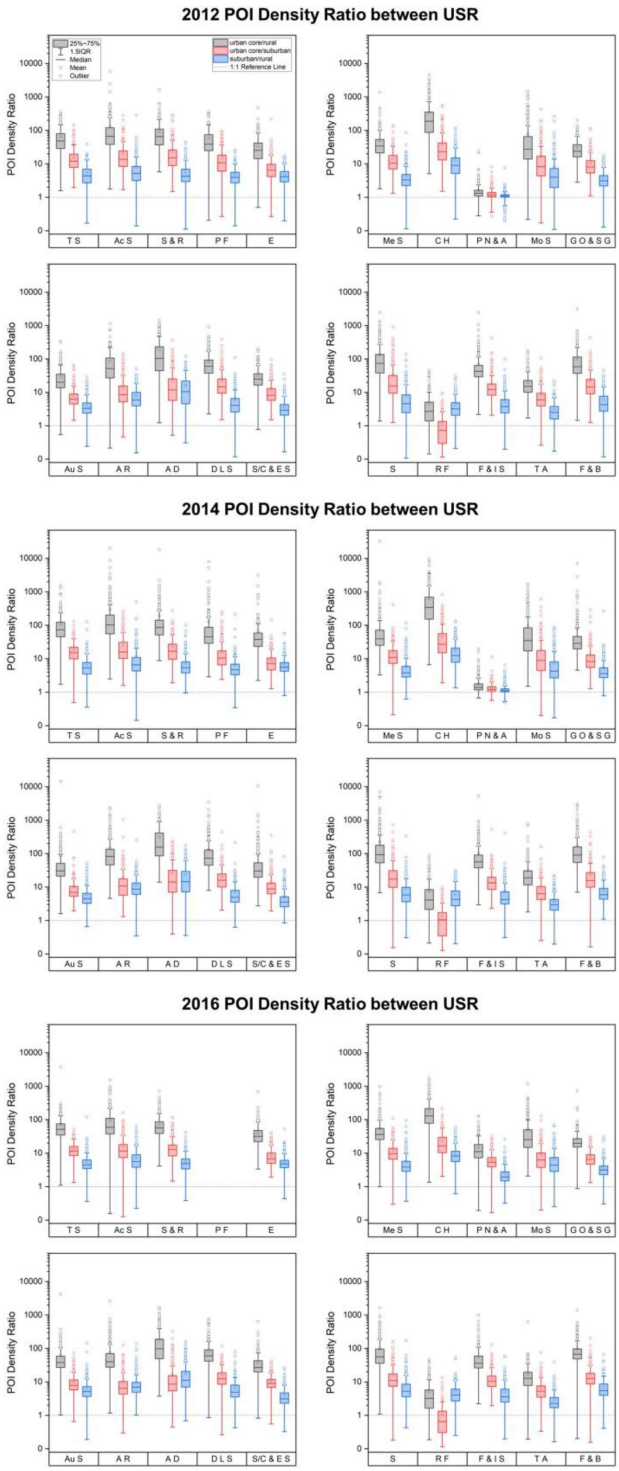

Fig. 7. Variation of the POIs density in USR.

in recent years. Of the administrative units with the U&S area closer to the GUB area in 2018, 55% were more economically developed cities, including 23 provincial capitals and three municipalities (e.g., Xiamen, Guangzhou), where the impervious surface construction of the urban core area reached saturation and spread to the suburban areas with a considerable human activity growth. In 2018, 45% of these cities were small cities, where the suburban areas were likely to be over-constructed as ghost towns with inconsistent economic development (e.g., Suzhou, Weihai, Jilin).

B. Comparison With Demographic Data

Considering that the USR structure was delineated based on the distinction of socio-economic conditions, we applied a population indicator from the GPW to evaluate its reliability. The respective total GPW gridded population for the USR of each administrative unit were calculated. Although the relationship between the USR area and their total population was complex, a generally linear pattern was observed between them after logarithmization. As shown in Fig. 6, the r values for the urban core were greater than 0.84, with the R^2 values greater than 0.7. The r values for the suburban and the rural were lower, but exceeded 0.75, with the R^2 values greater than 0.57. These results were better than those reported by Zhao et al. [18], which may also indicate the general significance of the USR datasets and the rationality of our USR datasets. Further, we evaluated the temporal patterns of the linear fit slopes for the three USR subcategories. The slope values (1.46–1.60) for the urban core were always the largest, with a decreasing trend observed during 2000–2020. This was consistent with the trend of intense people concentration in the urban core region with rapid urbanization in China. However, the rate of population concentration in the urban core gradually decreased in recent years. In the suburban areas, the slopes showed an increasing trend (1.06–1.21). This was consistent with the general cognition that the surplus population is moving from the densely populated urban cores to the suburban areas. It indicated that our time-series USR dataset was consistent with the gridded population dataset.

C. Comparison With POI Data

Urbanization is essentially associated with the construction of various infrastructures that can be indicated by POI data [60]. The POI dataset has been proven to be efficient in zoning urban areas as they cover all aspects of human activities [61], which makes it suitable for validating the USR results. In this study, we first examined the linear relationship between the USR areas and the number of POI in the corresponding subregion (see Table II). The results showed that the correlation in the urban core area was generally strongest among the three USR subcategories, with the median and the mean of r values being greater than 0.7. Further, the median and the mean of r values in rural areas were slightly greater than 0.5. The lowest correlation was found in suburban areas (the mean of r values was less than 0.5). This weak correlation in the suburban areas and the rural areas was reasonable because of the complex processes of urban expansion and infrastructure construction, which not only interact with each other but also are influenced by other factors, such as economic growth, population, governance, planning controls, and environmental characteristics. Considering that the relationship between POI and human activities can be significantly indicated by the spatial distribution of POI densities [61], we calculated the point densities of 20 categories of POI in each USR subregion and analyzed the POI density

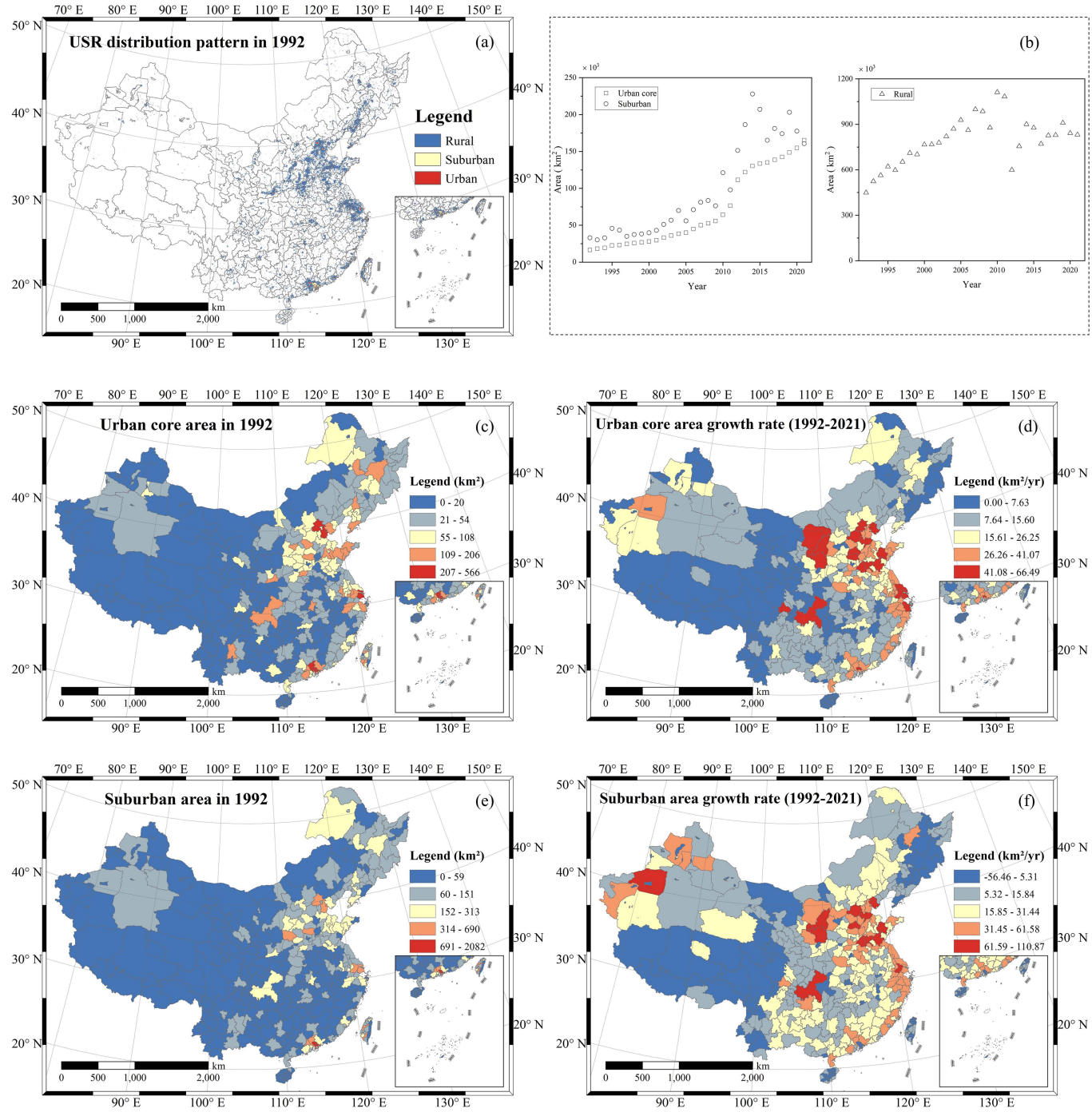

Fig. 8. (a) USR spatial distribution pattern in 1992. (b) Total USR areas changing pattern. (c) Every administrative unit's urban core area in 1992. (d) Every administrative unit's urban core area growth rate from 1992 to 2021. (e) Every administrative unit's suburban area in 1992. (f) Every administrative unit's suburban area growth rate from 1992 to 2021.

ratios for each category in the three USR subregions to evaluate the USR dataset. Our time-series USR extents delineated from NTL imagery were almost consistent with POI densities (see Fig. 7).

Except for the road furniture (RF) and the place name and address (PN&A), the POI density for other categories decreased significantly from the urban core areas to the rural areas. The RF (e.g., high-speed toll booths, high-speed service areas and so on) are usually found on highways connecting the inner-city areas to the outer areas, which are usually located in the suburban areas with less human activity, not in the urban core with dense human activity. Therefore, its density was highest in the suburban areas, followed by the urban core areas, and was lowest in the rural areas. The densities of the other 18 types of POI in the urban core were approximately 50 times higher than that in the rural and was 10 times higher than that in the suburban. The 18 POIs include all aspects of human life, which are closely related to human activities, so the densities of these POIs were naturally

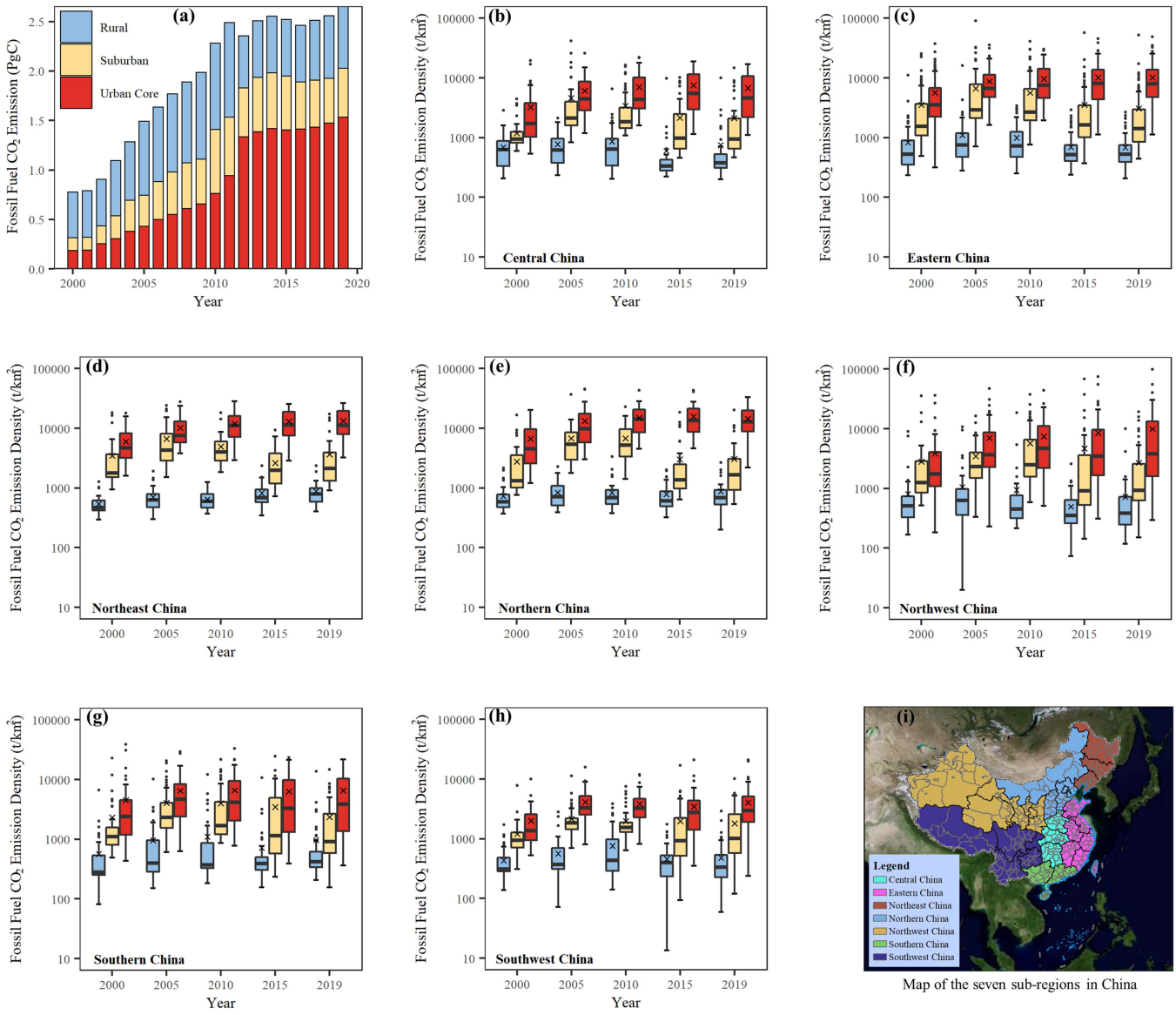

Fig. 9. Heterogeneity and the trend of ffco2 emissions in USR. (a) Total ffco2 emissions in USR. (b)–(h) ffco2 emission densities in USR among the seven sub-regions of China. (i) Map of seven sub-regions in China.

TABLE III
MEDIAN FFCO2 EMISSION DENSITIES IN USR OF SEVEN MAJOR REGIONS OF CHINA

		2000	2001	2002	2003	2004	2005	2006	2007	2008	2009	2010	2011	2012	2013	2014	2015	2016	2017	2018	2019
Central China (49)	urban core	1728.51	1917.03	3142.08	3748.36	4671.10	4441.54	4334.68	4198.41	4649.26	4662.91	4392.22	4713.47	5596.58	5235.11	5990.61	5513.28	6202.11	6149.12	6900.63	4624.38
	suburban	950.38	1054.07	1083.19	1462.84	1595.55	2132.72	1875.21	1824.35	2103.22	2075.25	1849.10	1923.92	1034.94	1056.53	1001.45	979.80	955.56	936.07	854.00	943.30
	rural	629.72	467.12	481.57	549.90	522.67	619.07	626.57	562.78	579.98	898.89	640.23	695.09	416.84	380.97	363.92	334.57	387.25	387.64	405.64	379.04
Eastern China (97)	urban core	3546.75	3580.88	4877.71	5342.78	5722.98	6732.64	6752.20	7020.02	7404.26	7652.78	7631.58	8648.56	9230.70	9108.22	8576.65	8102.83	8394.74	8028.15	8257.66	8025.31
	suburban	1549.69	1704.20	2294.12	2436.91	2695.72	2938.29	2931.36	2722.54	3631.76	2724.19	2669.63	2644.92	1752.15	1685.04	1658.56	1630.59	1527.56	1492.69	1440.32	1421.62
	rural	528.60	543.87	503.26	531.63	681.44	749.05	787.68	729.50	733.64	974.64	722.74	781.91	671.35	612.82	551.31	522.51	568.41	541.27	581.23	527.18
Northeast China (36)	urban core	4689.71	4412.27	4462.00	5074.42	6591.92	7567.68	8215.52	8871.71	8219.24	8186.03	11058.06	11165.43	11921.18	11199.84	11207.94	11392.62	11468.28	11258.44	11386.74	11133.78
	suburban	1786.14	1973.40	1625.77	2487.02	3414.40	4335.74	3603.42	3309.78	3729.90	2999.56	4025.11	3665.10	1824.66	3070.47	2202.70	1990.33	2075.06	1929.37	2145.78	2116.46
	rural	464.05	511.09	493.58	609.28	517.35	626.60	753.76	588.80	608.20	613.07	596.90	661.60	1667.96	937.94	725.25	684.97	831.86	792.47	887.38	799.77
Northern China (36)	urban core	4510.66	4535.22	4996.07	5472.58	9149.37	9861.78	11791.23	9839.87	14099.17	10397.22	14316.88	15925.68	13967.62	13745.26	13353.28	13642.44	13329.61	12610.30	12839.27	12847.60
	suburban	1318.85	1618.45	3266.56	3557.75	4335.19	5383.07	5181.11	6244.27	4750.77	5950.02	5258.05	5884.90	2039.69	2023.88	1645.96	1373.05	2025.85	1868.18	1959.56	1654.36
	rural	585.32	623.22	599.45	711.98	634.00	717.98	766.89	719.90	786.47	860.44	693.97	760.29	1109.20	776.34	549.94	610.07	696.63	687.74	698.40	693.19
Northwest China (62)	urban core	1738.27	1930.52	2191.52	2528.42	3601.06	3661.88	4008.96	4108.62	3939.33	4219.93	4664.98	3887.50	4278.79	4138.95	3996.06	3634.95	3646.26	3597.76	3998.32	3777.57
	suburban	1243.59	1122.74	1202.95	1522.14	1567.41	2331.98	2403.82	2565.31	2033.61	1853.57	2501.06	2675.25	1314.89	1846.07	902.37	919.96	953.12	880.82	896.78	929.58
	rural	511.07	512.80	490.21	546.13	536.60	626.29	698.51	649.86	661.80	764.94	451.72	590.54	572.13	457.42	303.60	352.58	409.47	432.74	423.99	383.32
Southern China (56)	urban core	2387.11	2579.39	2538.63	2895.06	3163.32	4695.45	4925.53	4958.30	4943.83	5098.10	4128.54	4224.40	3798.40	3470.38	3851.07	3296.78	3596.10	3642.56	3859.35	3842.68
	suburban	1108.02	1000.33	1044.46	1269.42	1133.51	2334.87	2233.35	2034.94	2225.89	2147.31	1678.61	1747.64	1029.23	1171.20	1101.84	1154.38	1002.46	1061.91	905.49	906.19
	rural	278.21	301.00	296.84	358.65	329.88	397.65	402.82	378.25	383.64	502.16	373.48	420.51	505.96	429.01	404.40	388.43	423.88	428.98	386.46	422.51
Southwest China (54)	urban core	1378.26	1394.16	2126.22	2393.43	2670.46	3327.32	3391.56	3458.62	3730.81	3711.99	3255.46	3186.25	3120.87	2737.07	2861.02	2794.40	2901.98	2781.43	2888.39	2988.22
	suburban	952.45	830.02	1056.02	1174.34	1180.28	1861.60	1719.73	1610.09	1658.08	1581.59	1555.81	1625.07	1033.18	879.29	892.36	935.90	838.24	896.23	908.14	1007.26
	rural	310.85	310.76	318.35	343.56	360.61	370.73	440.66	400.75	506.72	575.42	434.77	550.68	410.19	342.30	325.36	401.38	367.10	395.23	394.91	335.47

TABLE IV
MEAN FFCO2 EMISSION DENSITIES IN USR OF SEVEN MAJOR REGIONS OF CHINA

		2000	2001	2002	2003	2004	2005	2006	2007	2008	2009	2010	2011	2012	2013	2014	2015	2016	2017	2018	2019
Central China (49)	urban core	3250.98	3355.27	3960.58	4832.98	5882.99	6076.95	6388.88	6323.12	6849.94	6992.72	7068.44	6985.57	7916.17	7408.96	7629.47	7534.70	7419.22	7365.92	7651.84	6760.43
	suburban	1197.58	1382.41	2158.87	2164.40	3026.64	4613.37	3914.84	3879.00	4226.22	4209.09	3422.28	4201.27	3283.23	3238.83	2905.95	2168.86	2373.29	2009.68	1730.87	2136.78
	rural	690.09	611.44	619.71	731.88	769.74	776.09	846.03	747.91	770.82	1244.81	869.42	1006.27	524.81	538.96	511.37	603.25	754.53	743.12	824.03	746.52
Eastern China (97)	urban core	6674.23	6425.52	7490.73	8199.93	8612.39	9750.79	9890.42	10207.57	10344.46	10562.24	10642.88	11625.24	11349.24	11313.25	10838.02	10269.10	10289.96	10262.29	10203.44	10232.86
	suburban	3550.20	3184.09	4642.30	4397.44	4752.85	6686.26	5781.29	5083.74	5791.74	7066.67	5648.94	5457.19	3908.36	3583.97	3486.10	3525.68	3652.16	3412.90	3205.82	3078.14
	rural	837.67	948.78	863.83	1048.87	979.27	1101.07	1117.40	1083.83	1134.26	1211.39	1000.99	1207.74	858.90	790.66	722.29	704.61	751.23	721.07	788.75	687.95
Northeast China (36)	urban core	6026.88	6005.63	7607.16	7820.97	9767.59	10266.22	10771.32	12135.30	11748.12	10736.10	11993.16	12334.56	13551.22	12966.52	12813.07	13071.48	12707.21	12830.62	12625.85	13319.02
	suburban	3495.53	3429.96	3086.55	3801.98	5775.54	6704.58	5630.55	5028.14	5409.85	5364.50	4984.51	5893.63	6419.85	4534.89	3511.76	2637.55	3998.08	3723.43	4253.64	3691.74
	rural	543.35	598.86	584.79	670.10	573.31	701.02	837.08	627.21	666.07	720.51	640.99	735.31	2668.09	1085.89	788.45	815.69	886.19	894.74	1009.43	883.20
Northern China (36)	urban core	6643.41	6304.82	7891.55	8719.94	11051.99	13365.85	13978.77	12239.83	14459.24	13441.80	15121.66	17108.94	16298.98	15673.56	15677.29	15771.63	14899.41	14594.22	14625.42	14557.20
	suburban	2781.91	2903.33	4627.00	5201.19	6403.43	6834.44	6469.41	7623.11	6049.80	8736.50	6820.97	7014.62	4980.17	3766.97	2735.51	3023.50	3116.90	3091.91	3407.67	3088.00
	rural	742.35	812.89	768.02	964.45	761.66	843.25	1043.56	866.58	932.41	1064.88	839.59	941.42	1533.02	1017.09	714.58	788.57	887.08	962.70	965.18	878.39
Northwest China (62)	urban core	3841.15	4064.50	4655.51	5434.25	6431.30	7087.55	7415.47	7521.70	7526.40	7519.19	7443.14	7220.64	11560.78	11010.20	10647.41	10122.19	10231.45	9772.15	9956.95	9946.06
	suburban	2837.83	2927.16	2009.75	2572.14	2602.54	3484.73	3722.12	4533.49	5843.34	4205.61	5723.68	9261.75	5655.62	4490.23	3772.77	4702.36	3757.09	2668.34	3621.18	2700.92
	rural	805.17	688.76	800.83	923.78	812.35	1060.92	1096.85	938.23	857.49	1534.05	939.88	830.23	781.72	569.77	415.54	496.46	668.78	818.64	729.30	723.38
Southern China (56)	urban core	4513.82	4548.63	4656.04	4901.72	5157.70	6508.53	6753.01	6689.61	6781.82	7189.59	6631.77	6829.75	7274.76	6834.37	6567.99	6293.78	6733.61	6149.96	6528.52	6573.55
	suburban	2336.66	1555.77	1880.52	2716.04	2618.53	4070.30	4375.14	4300.33	5038.24	4575.81	4036.19	4482.50	2863.15	2981.69	2758.85	3488.27	2680.42	3038.79	2814.40	2354.87
	rural	569.37	621.51	659.97	752.50	759.41	959.63	935.29	995.31	989.75	1237.61	1109.06	1203.22	1013.19	881.83	937.74	728.37	937.41	873.62	839.65	969.54
Southwest China (54)	urban core	2003.38	1934.19	2412.12	2737.56	3059.67	4174.39	4175.86	4001.73	4387.74	4376.54	3895.70	3887.75	4394.98	3447.61	3311.59	3476.34	3616.57	3957.03	3957.40	4067.49
	suburban	1212.93	985.18	1694.16	1765.84	2055.37	2180.40	2042.27	2026.21	2050.91	1908.47	1976.23	2212.44	1934.34	1860.96	1907.97	1970.57	2034.05	1800.86	1908.20	1827.91
	rural	436.80	467.69	422.10	467.03	545.26	571.05	755.08	627.29	800.10	979.24	760.13	884.71	449.30	440.06	526.59	460.88	480.23	544.55	562.92	487.56

higher in places where the human activity intensity was higher. Comparison with the POI data showed that our USR product reflected the spatial differences of socio-economic and human activities well.

V. ANALYSIS AND ENVIRONMENTAL CASE STUDY

A. *Spatiotemporal Patterns of the USR*

The USR was mainly distributed in Northern China, Eastern China, and Southern China, forming contiguous regions in the middle and lower reaches of the Yellow River, Yangtze River Delta, and Pearl River Delta [see Fig. 8(a)]. During 1992–2021, all three USR subcategories in China showed an increasing trend [see Fig. 8(b)]. The urban core area increased from 16 000 km^2 in 1992 to 160 000 km^2 in 2021, and its proportion of the national land surface area increased almost 9-fold from 0.17% to 1.7%. The suburban area increased from 33 000 km^2 in 1992 to 160 658 km^2 in 2021. The rural areas increased from 450 000 km^2 in 1992 to about 800 000 km^2 in recent years. To investigate the size and the growth rate of the urban core area and the suburban area for each administrative unit, we used the natural breakpoint method to divide them into five categories [see Fig. 8(c)–(f)]. Eastern coastal cities had smaller initial urban core areas but higher growth rates. Further, cities in the middle and lower reaches of the Yellow River, Yangtze River Delta, and Pearl River Delta had smaller suburban areas, but most showed higher growth rates.

B. *Application in ffco2 Emissions Spatiotemporal Pattern*

CO_2 is one of the main greenhouse gases produced by humans [62]. CO_2 emissions from the fossil fuel combustion are the main cause of the increase in atmospheric CO_2 concentration [63]. This study applied the derived USR datasets and ODIAC data to investigate the total emissions and the density variations of ffco2 with distinct human activities. The total annual ffco2 emissions in billions of tons (PgC) were counted for the USR. The ffco2 emissions are divided by the respective area of the USR to obtain the respective annual ffco2 emissions density in t/km2 for each administrative unit. As shown in Fig. 9(a), the total ffco2 emissions of the USR increased from 0.78 PgC in 2000 to 2.65 PgC in 2019, expanding about 2.4 times and fluctuating around 2.5 PgC in recent years. The total ffco2 emissions in the urban core area rose from 0.19 PgC in 2000 to 1.53 PgC in 2019, up nearly 7.2 times, with the proportion rising from 24% to 58%. The total ffco2 emissions in the suburban area rose from 0.13 PgC in 2000 to 0.49 PgC in 2019, up nearly 2.8 times, with the proportion fluctuating around 20%. The ffco2 emissions in the rural area rose from 0.46 PgC in 2000 to 0.63 PgC in 2019, up nearly 0.4 times, and the proportion decreased from 59% to 24%. The ffco2 emissions of the USR have also stabilized in recent years, around 1.4 PgC, 0.5 PgC, and 0.6 PgC, respectively. The ffco2 emissions in USR have risen less rapidly than the expansion of the USR areas.

In order to make the ffco2 emissions of the USR comparable, which belong to different administrative units and have different areas, we used the total amount of ffco2 emissions divided by the area to calculate the ffco2 emission density to express the ffco2 emission intensity. As shown in Fig. 9(b)–(h), the distribution of ffco2 emission intensity in USR varies significantly among the seven sub-regions of China, which is larger in the urban core and smaller in the rural. The mean values of ffco2 emission intensity (the cross symbols in Fig. 9) were larger than the median (the black line in the box in Fig. 9), and the distribution showed some skewness. In general, the ffco2 emission density median in the urban core showed a trend of rising and then stabilizing, and it was stable at around 12 000 t/km^2 in North China and Northeast China, around 8000 t/km^2 in East China, around 6000 t/km^2 in Central China, and around 3000 t/km^2 in Northwest, Southwest, and South China. The ffco2 emission density median in suburban and rural showed a trend of increasing and then decreasing, with the values in suburban being around the interval of 1000–2000 t/km^2 in recent years and the values in rural generally being less than 1000 t/km^2 (see Table III). Meanwhile, the change trend of the ffco2 emission density mean (see Table IV) is similar to the change trend of the median. The urban core area has been growing, but its ffco2 emission density leveled

off. The ffco2 emission density of suburban and rural showed a decreasing trend, while the area has been still expanding.

VI. Conclusion

In this study, we generated a Chinese annual USR extents dataset (1992–2021) using NTL observations. The advantage of this dataset is that it provides spatially explicit Chinese USR maps with long temporal coverage for depicting the dynamics of urban core, suburban, and rural areas associated with locally distinct human activity intensities. This dataset is the first long time-series USR triad structure dataset of human settlements in China, which will benefit studies on environmental research issues. The USR dataset is free to download at https://dx.doi.org/10.21227/yzam-8z39. In this article, the derived USR dataset was compared and analyzed with the urban boundary data, the gridded demographic data, and the POI data. The results showed that the relationships between the urban core (or U&S) and the urban boundaries obtained from impervious surfaces exhibited spatial heterogeneity and different patterns of temporal change. The correlation coefficients between the population and the USR areas were greater than 0.75, which is better than the result of a previous study that delineated only urban extents. Further analysis showed that the suburban areas are important regions in China with an evident accelerated population increase in recent years. The derived USR dataset was also consistent with the POI density. The POI density in the urban core was 10 times higher than the suburban POI density and 50 times higher than the rural POI density. These evaluations indicated that this USR structure dataset was reliable for characterizing spatial extents associated with human settlements and distinct socio-economic activity intensity.

In addition, our results showed that the national urban core area increased nearly 9-fold from 16 000 km^2 in 1992 to 160 000 km^2 in 2021, while the national suburban area increased from 33 000 km^2 in 1992 to 160 000 km^2 in 2021 and decreased below the national urban core area for the first time in 2021. The national rural area increased and stabilized at approximately 800 000 km^2. Furthermore, the derived USR is beneficial to detailed analysis of USR disparities for various environmental issues (e.g., CO_2 emission). Based on the derived USR data, we found the ffco2 emission density showed a clear urban-rural gradient, and the extent of the difference was spatially heterogeneous. It is larger in the urban core and smaller in the rural. And it leveled off in the urban core and showed a decreasing trend in suburban and rural. This first long-time series USR dataset in China has potential in various environment and urbanization studies, such as those on CO_2 emission or those on urbanization patterns and the corresponding impacts on land use, habitat quality, urban heat islands, and urban climate.

References

[1] J. Qiu, "China vows to clean up rural environment," *Nature*, Apr. 2011, doi: 10.1038/news.2011.200.

[2] S. Liu, T. Chen, and J. Cai, "Peri-urbanization in China and its major research issues," *Acta Geographica Sinica*, vol. 59, no. 7s, pp. 101–108, Dec. 2004, doi: 10.11821/xb20047s014.

[3] B.-J. He, W. Wang, A. Sharifi, and X. Liu, "Progress, knowledge gap and future directions of urban heat mitigation and adaptation research through a bibliometric review of history and evolution," *Energy Buildings*, vol. 287, May 2023, Art. no. 112976, doi: 10.1016/j.enbuild.2023.112976.

[4] H. Liu et al., "Sensing-based park cooling performance observation and assessment: A review," *Building Environ.*, vol. 245, Nov. 2023, Art. no. 110915, doi: 10.1016/j.buildenv.2023.110915.

[5] H. Liu, B. He, S. Gao, Q. Zhan, and C. Yang, "Influence of non-urban reference delineation on trend estimate of surface urban heat island intensity: A comparison of seven methods," *Remote Sens. Environ.*, vol. 296, Oct. 2023, Art. no. 113735, doi: 10.1016/j.rse.2023.113735.

[6] A. Marques et al., "Increasing impacts of land use on biodiversity and carbon sequestration driven by population and economic growth," *Nature Ecol. Evol.*, vol. 3, no. 4, pp. 628–637, Apr. 2019, doi: 10.1038/s41559-019-0824-3.

[7] S. Angel, J. Parent, D. L. Civco, A. Blei, and D. Potere, "The dimensions of global urban expansion: Estimates and projections for all countries, 2000–2050," *Prog. Plan.*, vol. 75, no. 2, pp. 53–107, Feb. 2011, doi: 10.1016/j.progress.2011.04.001.

[8] W. Kuang, "National urban land-use/cover change since the beginning of the 21st century and its policy implications in China," *Land Use Policy*, vol. 97, Sep. 2020, Art. no. 104747, doi: 10.1016/j.landusepol.2020.104747.

[9] R. Mahtta et al., "Urban land expansion: The role of population and economic growth for 300+ cities," *npj Urban Sustain*, vol. 2, no. 1, Feb. 2022, Art. no. 5, doi: 10.1038/s42949-022-00048-y.

[10] H. Jiang et al., "Urban-rural disparities of carbon storage dynamics in China's human settlements driven by population and economic growth," *Sci. Total Environ.*, vol. 871, May 2023, Art. no. 162092, doi: 10.1016/j.scitotenv.2023.162092.

[11] X. Deng et al., "Exploring spatiotemporal pattern and agglomeration of road CO2 emissions in Guangdong, China," *Sci. Total Environ.*, vol. 871, May 2023, Art. no. 162134, doi: 10.1016/j.scitotenv.2023.162134.

[12] F. Zhao et al., "Urbanization–land-use interactions predict antibiotic contamination in soil across urban–rural gradients," *Sci. Total Environ.*, vol. 867, Apr. 2023, Art. no. 161493, doi: 10.1016/j.scitotenv.2023.161493.

[13] J. Xue, Q. Wang, and M. Zhang, "A review of non-point source water pollution modeling for the urban–rural transitional areas of China: Research status and prospect," *Sci. Total Environ.*, vol. 826, Jun. 2022, Art. no. 154146, doi: 10.1016/j.scitotenv.2022.154146.

[14] W. Yu et al., "Rural-urban disparities in the associations of residential greenness with diabetes and prediabetes among adults in southeastern China," *Sci. Total Environ.*, vol. 860, Feb. 2023, Art. no. 160492, doi: 10.1016/j.scitotenv.2022.160492.

[15] V. Gandla, M. Chiluka, H. Gupta, S. N. Sinha, and P. Chakraborty, "Sediment-water partitioning and risk assessment of organochlorine pesticides along the urban, peri-urban and rural transects of Krishna River Basin, Peninsular India," *Sci. Total Environ.*, vol. 874, May 2023, Art. no. 162360, doi: 10.1016/j.scitotenv.2023.162360.

[16] K. Robins et al., "Bioavailability of potentially toxic elements influences antibiotic resistance gene and mobile genetic element abundances in urban and rural soils," *Sci. Total Environ.*, vol. 847, Nov. 2022, Art. no. 157512, doi: 10.1016/j.scitotenv.2022.157512.

[17] R. Yuan, J. F. D. Rodrigues, J. Wang, A. Tukker, and P. Behrens, "A global overview of developments of urban and rural household GHG footprints from 2005 to 2015," *Sci. Total Environ.*, vol. 806, Feb. 2022, Art. no. 150695, doi: 10.1016/j.scitotenv.2021.150695.

[18] M. Zhao, C. Cheng, Y. Zhou, X. Li, S. Shen, and C. Song, "A global dataset of annual urban extents (1992–2020) from harmonized nighttime lights," *Earth System Sci. Data*, vol. 14, no. 2, pp. 517–534, Feb. 2022, doi: 10.5194/essd-14-517-2022.

[19] Y. Tian, J. Qian, and L. Wang, "Village classification in metropolitan suburbs from the perspective of urban-rural integration and improvement strategies: A case study of Wuhan, central China," *Land Use Policy*, vol. 111, Dec. 2021, Art. no. 105748, doi: 10.1016/j.landusepol.2021.105748.

[20] D. Lu, H. Tian, G. Zhou, and H. Ge, "Regional mapping of human settlements in southeastern China with multisensor remotely sensed data," *Remote Sens. Environ.*, vol. 112, no. 9, pp. 3668–3679, Sep. 2008, doi: 10.1016/j.rse.2008.05.009.

[21] J. Yang et al., "Contribution of urban ventilation to the thermal environment and urban energy demand: Different climate background perspectives," *Sci. Total Environ.*, vol. 795, Nov. 2021, Art. no. 148791, doi: 10.1016/j.scitotenv.2021.148791.

[22] J. Ren et al., "Exploring thermal comfort of urban buildings based on local climate zones," *J. Cleaner Prod.*, vol. 340, Mar. 2022, Art. no. 130744, doi: 10.1016/j.jclepro.2022.130744.

[23] Q. Wang, S. Wu, Y. Zeng, and B. Wu, "Exploring the relationship between urbanization, energy consumption, and CO2 emissions in different provinces of China," *Renewable Sustain. Energy Rev.*, vol. 54, pp. 1563–1579, Feb. 2016, doi: 10.1016/j.rser.2015.10.090.

[24] X. Luo, J. Yang, W. Sun, and B. He, "Suitability of human settlements in mountainous areas from the perspective of ventilation: A case study of the main urban area of Chongqing," *J. Cleaner Prod.*, vol. 310, Aug. 2021, Art. no. 127467, doi: 10.1016/j.jclepro.2021.127467.

[25] K. Anarfi, R. A. Hill, and C. Shiel, "Highlighting the sustainability implications of urbanisation: A comparative analysis of two urban areas in Ghana," *Land*, vol. 9, no. 9, Sep. 2020, Art. no. 300, doi: 10.3390/land9090300.

[26] J. R. Faria and A. Mollick, "Urbanization, economic growth, and welfare," *Econ. Lett.*, vol. 52, no. 1, pp. 109–115, Jul. 1996, doi: 10.1016/0165-1765(96)00839-7.

[27] K. Farrell, "The rapid urban growth triad: A new conceptual framework for examining the urban transition in developing countries," *Sustainability*, vol. 9, no. 8, Aug. 2017, Art. no. 1407, doi: 10.3390/su9081407.

[28] B.-J. He, "Cause-related injustice, process-related injustice, effect-related injustice and regional heat action planning priorities: An empirical study in Yangtze River Delta and Chengdu-Chongqing urban agglomerations," *Landscape Urban Plan.*, vol. 237, Sep. 2023, Art. no. 104800, doi: 10.1016/j.landurbplan.2023.104800.

[29] Y. Yang, M. Ma, C. Tan, and W. Li, "Spatial recognition of the urban-rural fringe of beijing using DMSP/OLS nighttime light data," *Remote Sens.*, vol. 9, no. 11, Nov. 2017, Art. no. 1141, doi: 10.3390/rs9111141.

[30] W. Lu, Y. Li, R. Zhao, and Y. Wang, "Using remote sensing to identify urban fringe areas and their spatial pattern of educational resources: A case study of the chengdu-chongqing economic circle," *Remote Sens.*, vol. 14, no. 13, Jan. 2022, Art. no. 3148, doi: 10.3390/rs14133148.

[31] Y. Zhou, X. Li, G. R. Asrar, S. J. Smith, and M. Imhoff, "A global record of annual urban dynamics (1992–2013) from nighttime lights," *Remote Sens. Environ.*, vol. 219, pp. 206–220, Dec. 2018, doi: 10.1016/j.rse.2018.10.015.

[32] B. Guindon, Y. Zhang, and C. Dillabaugh, "Landsat urban mapping based on a combined spectral–spatial methodology," *Remote Sens. Environ.*, vol. 92, no. 2, pp. 218–232, Aug. 2004, doi: 10.1016/j.rse.2004.06.015.

[33] A. Schneider, M. A. Friedl, and D. Potere, "Mapping global urban areas using MODIS 500-m data: New methods and datasets based on 'urban ecoregions'," *Remote Sens. Environ.*, vol. 114, no. 8, pp. 1733–1746, Aug. 2010, doi: 10.1016/j.rse.2010.03.003.

[34] L. Demarchi, F. Canters, J. C.-W. Chan, and T. Van de Voorde, "Multiple endmember unmixing of CHRIS/Proba imagery for mapping impervious surfaces in urban and suburban environments," *IEEE Trans. Geosci. Remote Sens.*, vol. 50, no. 9, pp. 3409–3424, Sep. 2012, doi: 10.1109/TGRS.2011.2181853.

[35] X. Li, P. Gong, and L. Liang, "A 30-year (1984–2013) record of annual urban dynamics of Beijing City derived from Landsat data," *Remote Sens. Environ.*, vol. 166, pp. 78–90, Sep. 2015, doi: 10.1016/j.rse.2015.06.007.

[36] A. Jacquin, L. Misakova, and M. Gay, "A hybrid object-based classification approach for mapping urban sprawl in periurban environment," *Landscape Urban Plan.*, vol. 84, no. 2, pp. 152–165, Feb. 2008, doi: 10.1016/j.landurbplan.2007.07.006.

[37] M. Herold, N. C. Goldstein, and K. C. Clarke, "The spatiotemporal form of urban growth: Measurement, analysis and modeling," *Remote Sens. Environ.*, vol. 86, no. 3, pp. 286–302, Aug. 2003, doi: 10.1016/S0034-4257(03)00075-0.

[38] K. E. Sawaya, L. G. Olmanson, N. J. Heinert, P. L. Brezonik, and M. E. Bauer, "Extending satellite remote sensing to local scales: Land and water resource monitoring using high-resolution imagery," *Remote Sens. Environ.*, vol. 88, no. 1, pp. 144–156, Nov. 2003, doi: 10.1016/j.rse.2003.04.006.

[39] Y. Huang, C. Wu, M. Chen, J. Yang, and H. Ren, "A quantile approach for retrieving the 'core urban-suburban-rural' (USR) structure based on nighttime light," *Remote Sens.*, vol. 12, no. 24, Jan. 2020, Art. no. 4179, doi: 10.3390/rs12244179.

[40] M. Zhao et al., "Applications of satellite remote sensing of nighttime light observations: Advances, challenges, and perspectives," *Remote Sens.*, vol. 11, no. 17, Jan. 2019, Art. no. 1971, doi: 10.3390/rs11171971.

[41] M. Zhao et al., "Mapping urban dynamics (1992–2018) in Southeast Asia using consistent nighttime light data from DMSP and VIIRS," *Remote Sens. Environ.*, vol. 248, Oct. 2020, Art. no. 111980, doi: 10.1016/j.rse.2020.111980.

[42] Y. Su et al., "A new method for extracting built-up urban areas using DMSP-OLS nighttime stable lights: A case study in the Pearl River Delta, southern China," *GIScience Remote Sens.*, vol. 52, no. 2, pp. 218–238, Mar. 2015, doi: 10.1080/15481603.2015.1007778.

[43] Y. Zhou, S. J. Smith, C. D. Elvidge, K. Zhao, A. Thomson, and M. Imhoff, "A cluster-based method to map urban area from DMSP/OLS nightlights," *Remote Sens. Environ.*, vol. 147, pp. 173–185, May 2014, doi: 10.1016/j.rse.2014.03.004.

[44] P. Sutton, D. Roberts, C. Elvidge, and K. Baugh, "Census from heaven: An estimate of the global human population using night-time satellite imagery," *Int. J. Remote Sens.*, vol. 22, no. 16, pp. 3061–3076, Jan. 2001, doi: 10.1080/01431160010007015.

[45] X. Li, L. Zhao, D. Li, and H. Xu, "Mapping urban extent using luojia 1-01 nighttime light imagery," *Sensors*, vol. 18, no. 11, Nov. 2018, Art. no. 3665, doi: 10.3390/s18113665.

[46] K. Shi, C. Huang, B. Yu, B. Yin, Y. Huang, and J. Wu, "Evaluation of NPP-VIIRS night-time light composite data for extracting built-up urban areas," *Remote Sens. Lett.*, vol. 5, no. 4, pp. 358–366, Apr. 2014, doi: 10.1080/2150704X.2014.905728.

[47] C. Small, F. Pozzi, and C. D. Elvidge, "Spatial analysis of global urban extent from DMSP-OLS night lights," *Remote Sens. Environ.*, vol. 96, no. 3, pp. 277–291, Jun. 2005, doi: 10.1016/j.rse.2005.02.002.

[48] P. Xiao, X. Wang, X. Feng, X. Zhang, and Y. Yang, "Detecting China's urban expansion over the past three decades using nighttime light data," *IEEE J. Sel. Topics Appl. Earth Observ. Remote Sens.*, vol. 7, no. 10, pp. 4095–4106, Oct. 2014, doi: 10.1109/JSTARS.2014.2302855.

[49] Z. Chen et al., "Mapping global urban areas from 2000 to 2012 using time-series nighttime light data and MODIS products," *IEEE J. Sel. Topics Appl. Earth Observ. Remote Sens.*, vol. 12, no. 4, pp. 1143–1153, Apr. 2019, doi: 10.1109/JSTARS.2019.2900457.

[50] J. Yang and Y. He, "Automated mapping of impervious surfaces in urban and suburban areas: Linear spectral unmixing of high spatial resolution imagery," *Int. J. Appl. Earth Observ. Geoinf.*, vol. 54, pp. 53–64, Feb. 2017, doi: 10.1016/j.jag.2016.09.006.

[51] T. Ma, Y. Zhou, C. Zhou, S. Haynie, T. Pei, and T. Xu, "Night-time light derived estimation of spatio-temporal characteristics of urbanization dynamics using DMSP/OLS satellite data," *Remote Sens. Environ.*, vol. 158, pp. 453–464, Mar. 2015, doi: 10.1016/j.rse.2014.11.022.

[52] T. Ma, Z. Yin, and A. Zhou, "Delineating spatial patterns in human settlements using VIIRS nighttime light data: A watershed-based partition approach," *Remote Sens.*, vol. 10, no. 3, Mar. 2018, Art. no. 465, doi: 10.3390/rs10030465.

[53] X. Li, Y. Zhou, M. Zhao, and X. Zhao, "A harmonized global nighttime light dataset 1992–2018," *Sci. Data*, vol. 7, no. 1, Jun. 2020, Art. no. 168, doi: 10.1038/s41597-020-0510-y.

[54] C. D. Elvidge, M. Zhizhin, T. Ghosh, F.-C. Hsu, and J. Taneja, "Annual time series of global VIIRS nighttime lights derived from monthly averages: 2012 to 2019," *Remote Sens.*, vol. 13, no. 5, Jan. 2021, Art. no. 922, doi: 10.3390/rs13050922.

[55] X. Li et al., "Mapping global urban boundaries from the global artificial impervious area (GAIA) data," *Environ. Res. Lett.*, vol. 15, no. 9, Aug. 2020, Art. no. 094044, doi: 10.1088/1748-9326/ab9be3.

[56] Center For International Earth Science Information Network-CIESIN-Columbia University, "Gridded population of the world, version 4 (GPWv4): Population count, revision 11," Palisades, New York, NY, USA: NASA Socioeconomic Data and Applications Center (SEDAC), 2018, doi: 10.7927/H4JW8BX5.

[57] P. Gong et al., "Annual maps of global artificial impervious area (GAIA) between 1985 and 2018," *Remote Sens. Environ.*, vol. 236, Jan. 2020, Art. no. 111510, doi: 10.1016/j.rse.2019.111510.

[58] Y. Huang, J. Yang, M. Chen, C. Wu, H. Ren, and Y. Liu, "An approach for retrieving consistent time series 'urban core–suburban-rural' (USR) structure using nighttime light data from DMSP/OLS and NPP/VIIRS," *Remote Sens.*, vol. 14, no. 15, Jan. 2022, Art. no. 3642, doi: 10.3390/rs14153642.

[59] M. Zhao et al., "Building a series of consistent night-time light data (1992–2018) in southeast Asia by integrating DMSP-OLS and NPP-VIIRS," *IEEE Trans. Geosci. Remote Sens.*, vol. 58, no. 3, pp. 1843–1856, Mar. 2020, doi: 10.1109/TGRS.2019.2949797.

[60] K. Liu, L. Yin, F. Lu, and N. Mou, "Visualizing and exploring POI configurations of urban regions on POI-type semantic space," *Cities*, vol. 99, Apr. 2020, Art. no. 102610, doi: 10.1016/j.cities.2020.102610.

[61] Q. Dong, S. Qu, J. Qin, D. Yi, Y. Liu, and J. Zhang, "A method to identify urban fringe area based on the industry density of POI," *ISPRS Int. J. Geo-Inf.*, vol. 11, no. 2, Feb. 2022, Art. no. 128, doi: 10.3390/ijgi11020128.

[62] T. Oda and S. Maksyutov, "A very high-resolution (1 km×1 km) global fossil fuel CO_2 emission inventory derived using a point source database and satellite observations of nighttime lights," *Atmospheric Chem. Phys.*, vol. 11, no. 2, pp. 543–556, Jan. 2011, doi: 10.5194/acp-11-543-2011.

[63] T. Oda, S. Maksyutov, and R. J. Andres, "The open-source Data Inventory for Anthropogenic CO_2, version 2016 (ODIAC2016): A global monthly fossil fuel CO_2 gridded emissions data product for tracer transport simulations and surface flux inversions," *Earth System Sci. Data*, vol. 10, no. 1, pp. 87–107, Jan. 2018, doi: 10.5194/essd-10-87-2018.

Biao Xiong was born in Xiantao, Hubei, China, in 2000. He received the B.S. degree in geographic information science from Lanzhou University, Lanzhou, China, in 2021. He is currently working toward the master's degree in geographic information science with the State Key Laboratory of Resources and Environmental Information System, Institute of Geographic Sciences and Natural Resources Research, Chinese Academy of Sciences, Beijing, China.

His research interests include ecological environment remote sensing and spatiotemporal data analysis.

Yaohuan Huang was born in Huangshan, Anhui, China, in 1982. He received the B.S. degree in physical geography from the Northeast Normal University, Changchun, China, in 2003, the M.S. degree in geographic information science from the Institute of Geographic Sciences and Natural Resources Research, Chinese Academy of Sciences, Beijing, China, in 2007, and the Ph.D. degree in hydrology and water resources from the China Institute of Water Resources and Hydropower Research, Beijing, China, in 2010.

Since 2013, he has been an Associate Professor with the State Key Laboratory of Resources and Environmental Information System, Institute of Geographic Sciences and Natural Resources Research, Chinese Academy of Sciences. His research interests include UAV remote sensing objects detection, spatial analysis, and land use/cover change and their interactions with climate change.

Mingxing Chen was born in Chaohu, Anhui, China, in 1982. He received the B.S. degree in human geography and the M.S. degree in geographic information science from the Anhui Normal University, Anhui, China, in 2003 and 2006, and the Ph.D. degree in human geography from the Institute of Geographic Sciences and Natural Resources Research, Chinese Academy of Sciences, Beijing, China, in 2009.

Since 2018, he has been a Professor with the Institute of Geographic Sciences and Natural Resources Research, Chinese Academy of Sciences. His research interests include urbanization and global change, regional development mode, and territorial spatial planning.

Chengbin Wu (Student Member, IEEE) was born in Kunming, Yunnan, China, in 1995. He received the B.S. degree in geographical information science from the China University of Petroleum, Qingdao, China, in 2018. He is currently working toward the Ph.D. degree in geographic information science with the State Key Laboratory of Resources and Environmental Information System, Institute of Geographic Sciences and Natural Resources Research, Chinese Academy of Sciences, Beijing, China.

From 2018 to 2019, he was a Research Assistant with the Key Laboratory of Digital Earth Science, Aerospace Information Research Institute, Chinese Academy of Sciences. His research interests include UAV remote sensing objects detection, spatial analysis, and geoscience inference.

Hongyan Ren was born in Yueyang, Hunan, China, in 1979. He received the B.S., M.S., and Ph.D. degrees in resources and environmental sciences from Nanjing Agricultural University, Nanjing, China, in 2002, 2005, and 2008, respectively. Since 2016, he has been an Associate Professor with the State Key Laboratory of Resources and Environmental Information System, Institute of Geographic Sciences and Natural Resources Research, Chinese Academy of Sciences. His research interests include historical reconstruction, modeling, and analysis of environmental change and health geography.